Longitudinal correlations from fluctuating strings in Pb-Pb, *p*-Pb, and *p*-*p* collisions

Martin Rohrmoser[*] and Wojciech Broniowski[†]
H. Niewodniczański Institute of Nuclear Physics PAN, 31-342 Cracow, Poland
and Institute of Physics, Jan Kochanowski University, 25-406 Kielce, Poland

(Received 9 September 2019; revised manuscript received 26 November 2019; published 10 January 2020)

In a framework of a semianalytic model with longitudinally extended strings of fluctuating endpoints, we demonstrate that the rapidity spectra and two-particle correlations in collisions of Pb-Pb, *p*-Pb, and *p*-*p* at the energies of the Large Hadron Collider can be universally reproduced. In our approach, the strings are pulled by wounded constituents appearing in the Glauber modeling at the partonic level. The obtained rapidity profile for the emission of hadrons from a string yields bounds for the distributions of the endpoint fluctuations. Then, limits for the two-particle correlations in pseudorapidity can be obtained. Our results are favorably compared to recent experimental data from the ATLAS Collaboration.

DOI: 10.1103/PhysRevC.101.014907

I. INTRODUCTION

Longitudinal correlations are an important source of information on the dynamics of hadronic collisions. There are numerous ongoing efforts to understand them, both on the theoretical side as well as in experiments at the BNL Relativistic Heavy-Ion Collider (RHIC) and the CERN Large Hadron Collider (LHC), in particular with detector upgrades covering broader ranges in pseudorapidity. As is well known, long-range rapidity correlations supply information on the earliest phases of the reaction, since from causality the correlations stem from proper times τ limited by $\tau \lesssim \tau_f \exp(-\Delta\eta/2)$, where τ_f is the freeze-out proper time and $\Delta\eta$ is the pseudorapidity separation of the particles in a pair.

In our recent paper [1] we presented an analysis of the longitudinal hadronic correlations at the highest RHIC energy of $\sqrt{s_{NN}} = 200$ GeV in the framework of a simple model where emission proceeds from strings with fluctuating endpoints [2]. The model is, up to emission profiles extracted from the data, analytic, which allows us a simple understanding of generic production features present in various string or flux-tube approaches. The present study provides an extension of our method to LHC energies.

We recall that QCD-motivated string or color flux-tube models are commonly used in particle physics phenomenology to describe the longitudinal dynamics. The strings extend between receding color sources and fragment, producing hadrons. Many sophisticated Monte Carlo codes are based on the Lund string model (see, e.g., [3–8]), or on the dual parton model built on the Pomeron and Regge exchanges [9–11]. A common feature of these phenomenologically successful codes is the formation of a collection of strings pulled between the constituents of the projectiles in the early stage of the collision. The endpoints of a string have opposite color charges (triplet-antitriplet for the quark-diquark and quark-antiquark configurations, or octet-octet for the gluon-gluon case). Moreover, the location of the string endpoints in spatial rapidity $\eta_{PS} \equiv \frac{1}{2}\ln[(t+z)/(t-z)]$ fluctuates, following a proper parton distribution function. As argued in Refs. [1,2], these fluctuations are the key feature enabling control over the one-body densities (pseudorapidity spectra) and the two-particle correlations in pseudorapidity. In our study we focus on this effect, neglecting other features typically incorporated in Monte Carlo codes, such as nuclear shadowing or baryon stopping. In our study, rather than using the parton distribution functions to describe the endpoint distributions, we take a more flexible and phenomenological approach, where these distributions are adjusted to reproduce the pseudorapidity spectra.

Another important issue is the distribution of the number of strings, which finally translates into the multiplicity of the produced hadrons. We use the fact that the multiplicity of the produced hadrons is successfully described within the wounded picture [12], which is an adoption of the Glauber theory [13] to inelastic collisions [14]. Moreover, the wounded quark scaling [15–18] has been shown to work surprisingly well [19–37] at both RHIC and LHC collision energies. Extensions to more partons per nucleon than just three quarks have also been considered, with the conclusion that the increase in energy yields more wounded partons [29]. In the present study we use the wounded model with a few (3 to 6) constituents per nucleon.

II. THE MODEL

As mentioned, our model combines the string picture with the wounded parton model, assuming that the number of strings is given by the number of wounded constituents. As a matter of fact, this complies with the Lund model mechanism, where the basic string extends between a parton from a given

[*]mrohrmoser@ifj.edu.pl
[†]wojciech.broniowski@ifj.edu.pl

nucleon and a parton (or diquark) from *the same* nucleon [3]. Thus, in collisions of nuclei A and B, hadrons are emitted from strings associated with mutually independent N_A wounded partons from A and N_B wounded partons from B, respectively. At a given collision energy the emission profile of hadrons (defined as the number of hadrons per η) from each string, $f(\eta)$, is assumed to be universal, i.e., independent of the mass numbers of the projectiles or centrality. Here η denotes the pseudorapidity in the center of mass of the colliding NN system. The above assumptions correspond to the following scaling law [38]:

$$\frac{dN_{\rm ch}}{d\eta} = \langle N_A\rangle f(\eta) + \langle N_B\rangle f(-\eta), \tag{1}$$

where we have adopted the convention that A moves to the right and B to the left along the z axis. The symbol $\langle\cdot\rangle$ denotes the average over events in the considered centrality class.

From Eq. (1) it follows that the symmetric and antisymmetric parts of the distributions are given by

$$\begin{aligned}\frac{1}{2}\left(\frac{dN}{d\eta}(\eta) + \frac{dN}{d\eta}(-\eta)\right) &= \langle N_+\rangle f_s(\eta),\\ \frac{1}{2}\left(\frac{dN}{d\eta}(\eta) - \frac{dN}{d\eta}(-\eta)\right) &= \langle N_-\rangle f_a(\eta),\end{aligned} \tag{2}$$

with $N_\pm = N_A \pm N_B$ denoting the sum and the difference of sources from A and B, whereas $f_s(\eta)$ and $f_a(\eta)$ denote the symmetric and antisymmetric parts of the profile $f(\eta)$.

In our simulations, centrality is determined via the quantiles of the total number of wounded partons, $\langle N_+\rangle$.

From various studies of hadron multiplicity distributions in p-Pb collisions, it is known that the Glauber approach of hadron production must be amended with fluctuations of the number of sources. Typically, the negative binomial distribution is overlaid over the distribution of wounded sources. We follow this scheme in our simulations, with the following prescription: we generate events with GLISSANDO 3 [39], with n_A and n_B wounded partons in a given event. Then we generate randomly $N_A = k(N_A; n_A, q)$ and $N_B = k(N_B; n_B, q)$, where

$$k(x; n, q) = \mathrm{NB}\left[x; \frac{nq}{1-q}, q\right] \tag{3}$$

is the negative binomial distribution with $x = 0$ removed, i.e., $x = 1, 2, 3, \ldots$. The cases where $N_A = 0$ or $N_B = 0$ (no strings) are disregarded. By construction, $\langle x\rangle = n$ and $\mathrm{var}(x) = n/q$. The parameter $q \leqslant 1$, treated as a free variable to be fitted, controls the variance of the number of strings.

The role of increased fluctuations introduced by an overlaid distribution enters indirectly into our analysis, by modifying the division of the event sample into centrality classes.

III. EXTRACTION OF THE EMISSION PROFILE FROM PSEUDORAPIDITY SPECTRA

This section explains in detail how the experimental data on rapidity spectra from p-Pb and Pb-Pb collisions at the LHC with $\sqrt{s_{NN}} = 5.02$ TeV were jointly fitted to obtain the emission profiles of Eq. (1). We carry out the following steps:

(1) Choose the variant of the model by deciding on the number of partons per nucleon.
(2) GLISSANDO 3 is run to generate event samples with the number of wounded sources n_A and n_B for both the p-Pb and Pb-Pb collisions.
(3) For a given value of, samples with string numbers N_A and N_B are obtained by overlaying a negative binomial distribution according to Eq. (3).
(4) The samples for p-Pb and Pb-Pb are then divided into centrality classes according to the values of N_+.
(5) The values of $\langle N_A\rangle$ and $\langle N_B\rangle$ in all centrality classes are used to construct the least-squares fit of the profiles $f(\eta)$ to the experimental pseudorapidity spectra $dN_{\rm ch}/d\eta$ from Eq. (1).
(6) Steps 3–5 are repeated to obtain the optimum value of q, corresponding to a global minimum of the least square function. The result is the optimum profile $f(\eta)$.

In the fitting procedure, the symmetric part of the profile, $f_s(\eta)$, is sensitive to both the Pb-Pb and p-Pb data, whereas the the antisymmetric part, $f_a(\eta)$, depends only on the (asymmetric) p-Pb collisions, as is obvious from Eq. (2). As we wish to fit jointly the Pb-Pb and p-Pb data, we choose the collision energy where both sets of data on the pseudorapidity spectra are available, namely $\sqrt{s_{NN}} = 5.02$ TeV. Specifically, we take ALICE data [40] on pseudorapidity spectra of Pb-Pb, and the ATLAS data [41] on pseudorapidity spectra of p-Pb. We note that the data used for the p-Pb pseudorapidity spectra for p-Pb collisions from ATLAS [41] are accurately compatible with the ALICE [40] data with the V0A selection of centrality. We prefer to use the ATLAS data here, as we will compare the results of our model with the pseudorapidity correlations extracted from the ATLAS experiment [41].

The experimental data for p-Pb collisions at the LHC are shifted with respect to the NN center-of-mass frame by 0.465 units of rapidity. Since rapidity y and pseudorapidity η are related as $p_T \sinh(\eta) = \sqrt{m^2 + p_T^2}\sinh(y)$, where p_T is the transverse momentum and m the particle's mass, one can obtain $\eta \approx y$ in the case $m \ll p_T$, which we assume in our further considerations. One can justify this assumption by the fact that the emitted particles are predominantly pions with a small rest mass of $m_\pi \simeq 140$ MeV, which is smaller than typical values of p_T. Thus, to a good approximation

TABLE I. Optimum values of the negative binomial parameter q and the corresponding value of the least-squares function $\hat{L}$, for models with various numbers of partons per nucleon.

Constituents	q	$\hat{L}$
3	0.245	476
4	0.905	140
5	0.785	137
6	0.805	571

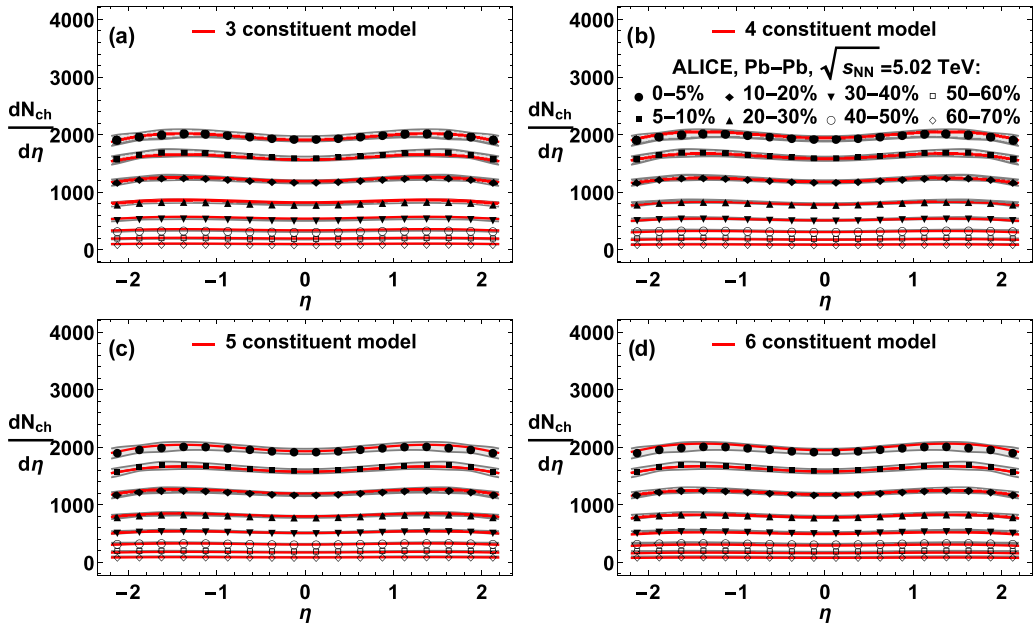

FIG. 1. Model results (solid lines) and ALICE data [40] (points with bands indicating experimental errors) for the pseudorapidity spectra in Pb-Pb collisions at 5.02 TeV. Subsequent panels correspond to models with 3, 4, 5, and 6 partons per nucleon.

the pseudorapidity η in the laboratory frame is related to η in the NN center-of-mass (CM) frame, $\eta_{\rm lab} \simeq \eta_{\rm CM} + 0.465$. This allows us to transform the experimental pseudorapidity spectra from p-Pb collisions into the CM frame by a simple shift.

A joint least-squares fit for Pb-Pb and p-Pb spectra can be performed in the following way: For each value of q individually the numbers of sources in the wounded parton model, overlaid with the negative binomial distribution, are generated with the help of GLISSANDO 3 [39]. In order to obtain the emission profile $f(\eta)$ we construct for each value of η for which the data exists the least squares sum $L(f_A(\eta), f_B(\eta))$, depending on two fitting parameters $f_A(\eta)$ and $f_B(\eta)$:

$$L(f_A(\eta), f_B(\eta)) = \frac{1}{N}\sum_{i=1}^{N}\left\{\left[\left(\frac{dN}{d\eta}(\eta)\right)_i - [\langle N_A\rangle_i f_A(\eta) + \langle N_B\rangle_i f_B(\eta)]\right]^2 + \left[\left(\frac{dN}{d\eta}(-\eta)\right)_i - [\langle N_B\rangle_i f_A(\eta) + \langle N_A\rangle_i f_B(\eta)]\right]^2\right\}, \quad (4)$$

where i runs over all spectra (i.e., all the centrality classes and reactions) that are to be fitted.[1] We then minimize $L(\eta, f_A, f_B)$ at each η, which yields the functions $f_A(\eta)$ and $f_B(\eta)$. Our choice for the least-squares sum, Eq. (4), has the desired symmetry property $L(-\eta, f_A, f_B) = L(\eta, f_B, f_A)$, which follows from the fact that $f_A(\eta) = f_B(-\eta)$, which means the replacement of the left-going wounded source by the right-going one. Recall that in the notation of Eq. (1) $f(\eta) = f_A(\eta) = f_B(-\eta)$.

[1]We use all the available rapidity spectra for Pb-Pb and p-Pb, except the p-Pb data for the most central 1% of collisions, which are far off the optimal fit, hinting at different physics in this case.

The procedure described above provides the optimum emission spectrum $f(\eta)$ for a given value of the negative binomial parameter q of Eq. (3). To obtain the optimum value of q we additionally minimize the least-squares sum (4) summed over all values of η, denoted as $\hat{L}$, with respect to q. The optimum values for q for the models with 3, 4, 5, and 6 partons per nucleon together with the corresponding values for the least-squares sum $\tilde{L}$ are listed in Table I. We note that the values for $\tilde{L}$ are lowest for models with 4 or 5 constituents per nucleon. Thus in the following we focus on results for these two cases.

The results of our fits for the symmetric parts of the Pb-Pb pseudorapidity spectra for the models with 3, 4, 5, and 6 partons per nucleon are shown in Fig. 1. As the figure shows, the ALICE data [40] are reasonably well reproduced for all variants of the model and for all centrality selections. Thus the Pb-Pb spectra do not discriminate between the variants of the model.

The situation is different for the p-Pb case. Figures 2 and 3 show, respectively, the symmetric and antisymmetric parts of the pseudorapidity spectra for p-Pb collisions, compared the ATLAS data [41]. Whereas for the antisymmetric contributions, shown in Fig. 3, all variants of the model reproduce the data reasonably well, significant differences can be noticed in the symmetric contributions, shown in Fig. 2. Acceptable agreement is obtained for 4 and 5 partons. In the following parts of this article, when considering correlations, we will thus focus on the 4 and 5 parton cases.

The corresponding universal profiles $f(\eta)$ obtained from our fitting procedure are shown in Fig. 4, together with their symmetric and antisymmetric contributions $f_s(\eta)$ and $f_a(\eta)$ given in Fig. 5. We note from Fig. 4 that the profiles scaled by the central value, $f(\eta)/f(0)$, differ by a few percent at peripheral values of η, with a steeper fall-off with η for larger number of partons per nucleon.

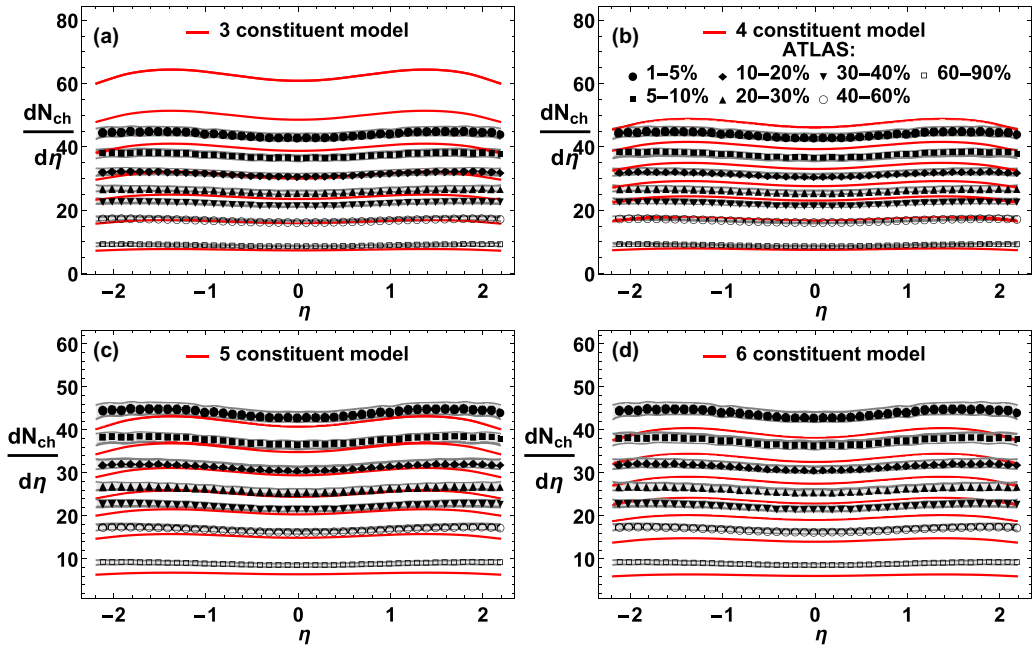

FIG. 2. Model results (solid lines) and ATLAS data [41] (points with bands indicating experimental errors) for the symmetric parts of the pseudorapidity spectra in p-Pb collisions at 5.02 TeV. Subsequent panels correspond to models with 3, 4, 5, and 6 partons per nucleon.

Figure 5(a) shows that the symmetric parts of the profiles, $f_s(\eta)$, decrease with the number of partons. This behavior is natural and follows from the first of Eqs. (2). When $\langle N_+ \rangle$ decreases due to a smaller number of partons per nucleon, the magnitude of $f_s(\eta)$ needs to be correspondingly increased to yield the same pseudorapidity spectra. Figure 5(b) shows the antisymmetric parts of the profiles, $f_a(\eta)$. As can be seen, the different number of partons per nucleon has essentially no influence on $f_a(\eta)$. We have found no apparent physical reason for such a behavior, which may be considered accidental. The overall steeper fall-off of profiles $f(\eta)/f(0)$ in Fig. 4 with increasing number of partons per nucleon can thus be understood via the decrease of the magnitude of $f_s(\eta)$, with no change in $f_a(\eta)$.

We remark that instead of the least-squares sum of Eq. (4) we can use the χ^2 function, which yields essentially the same optimum results. Regarding the values of χ^2/d.o.f., admittedly they are large due to the approximate nature of our

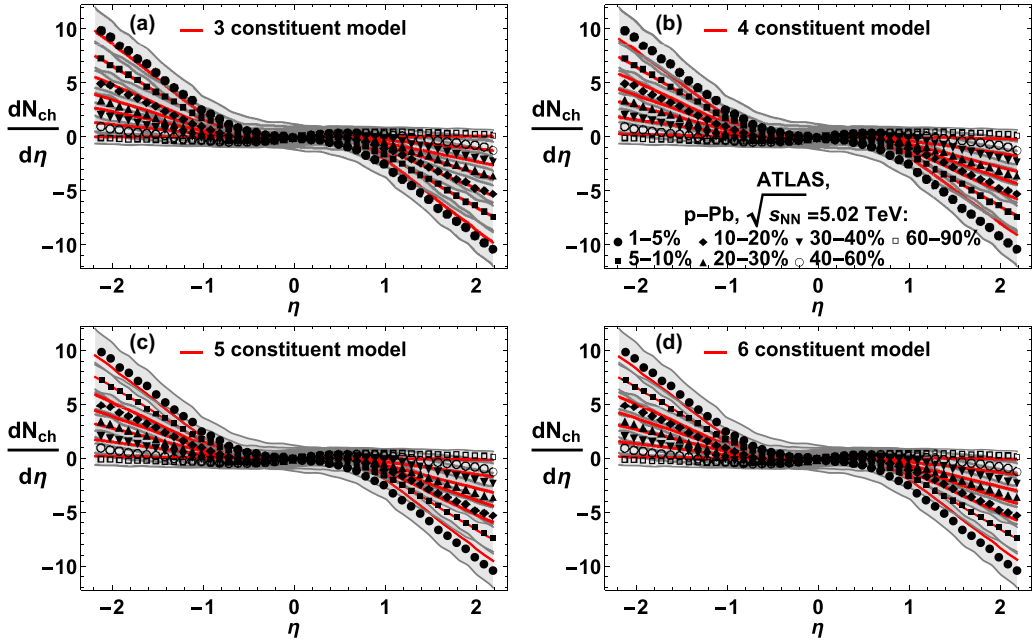

FIG. 3. Same as in Fig. 2, but for the antisymmetric part of the p-Pb spectra.

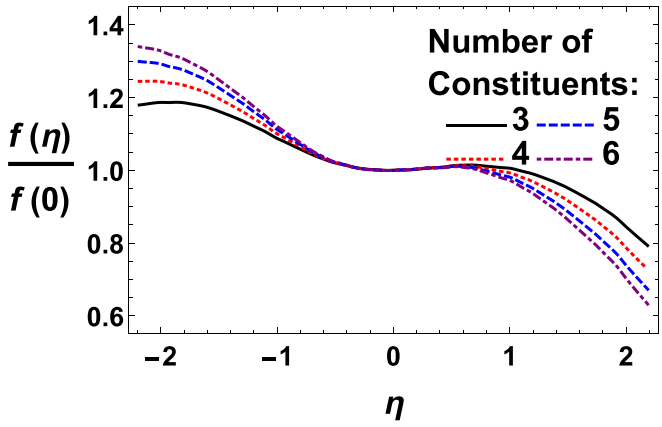

FIG. 4. Emission profile in pseudorapidity, divided by its value at the origin, $f(\eta)/f(0)$, for models with various numbers of constituents per nucleon.

model, which assumes a very simple uniform mechanism of string production and breaking. Thus the values of χ^2/d.o.f. cannot be used as stringent measures of the statistical quality of the fit, which is an issue shared by many models applied to ultrarelativistic nuclear collisions.

To conclude this section, as a preliminary step of our study we were able to uniformly fit in an approximate way the experimental data for Pb-Pb and p-Pb collisions from the ALICE [40] and ATLAS [41] Collaborations, respectively, in the wounded parton model, with a preference for a model variant with 4 or 5 wounded constituents per nucleon.

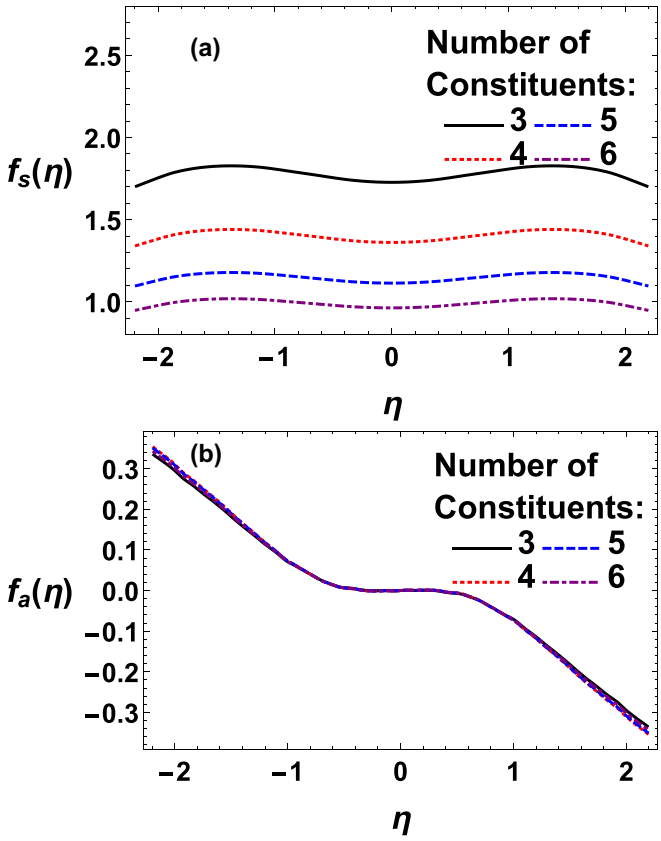

FIG. 5. Symmetric (a) and antisymmetric (b) parts of the emission profile $f(\eta)$ for models with various numbers of constituents per nucleon.

IV. STRING END-POINT DISTRIBUTIONS

In this section we proceed in analogy to our earlier work [1]. However, in contrast to the description used therein, in this article we pass from the profile functions in pseudorapidity η, obtained in the previous section, to the profile functions in rapidity y. The reason is technical but relevant. The method of [1] works for profile functions which are unimodal (have a single maximum), as this is what follows from strings continuously stretched between fluctuating endpoints. Unimodality is not the case in the present analysis, as can be seen from Fig. 4. For instance, for the case of 3 constituent partons per nucleon, one can notice a maximum at $\eta \simeq -1.8$ and another weak maximum at $\eta \simeq 0.8$ (variants with a larger number of constituents have a maximum outside of the left bound of the plot). However, the maximum near 0.8 is an artifact of using pseudorapidity rather than rapidity.

As can be seen from the experimental data [40–43], pseudorapidity spectra mainly differ from rapidity spectra by a pronounced dip around $\eta = 0$, which trivially follows from the kinematic relation between rapidity and pseudorapidity. In order to pass from pseudorapidity to rapidity for the spectra which are largely dominated by the pions, we use the simplifying assumption of a factorization of the rapidity and p_T dependence of the spectra. Then, approximately, one can write

$$\frac{dN}{dy} = \int dp_T \frac{d\eta(y, p_T, m_\pi)}{dp_T dy} \frac{dN}{d\eta} \approx \frac{d\eta}{dy} \frac{dN}{d\eta}\bigg|_{y\approx\eta}. \quad (5)$$

The Jacobian $d\eta/dy$ in the last part of Eq. (5) can be obtained from the experimental data from ALICE for the 5% most central Pb-Pb collisions [40], where both the rapidity, dN/dy, and pseudorapidity, $dN/d\eta$, spectra are provided. This procedure, in essence, is a way of averaging over the transverse momentum p_T, incorporating the experimental acceptance.

Consequently, we can obtain the one-body emission profiles $f(y)$ in terms of $f(\eta)$ presented in Sec. III, namely,

$$f(y) = \frac{d\eta}{dy} f(\eta). \quad (6)$$

Thus obtained result for $d\eta/dy$ is shown in Fig. 6. Similarly, for the two-particle emission profiles we get

$$f_2(y_1, y_2) = \frac{d\eta_1}{dy_1} \frac{d\eta_2}{dy_2} f_2(\eta_1, \eta_2), \quad (7)$$

which will be used in the next section.

The results for $f(y)$ in models with 3, 4, 5, and 6 wounded partons obtained with Eq. (6) are shown in Fig. 7. The feature that can be seen when comparing to $f(\eta)$ from Fig. 4 is the absence of the central dip in the symmetric part. As a result, $f(y)$ at various centralities are unimodal functions (have only one maximum at negative y), which allows us to carry out the

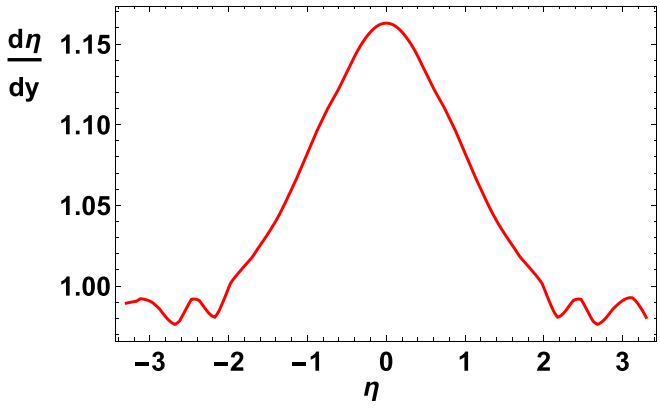

FIG. 6. The Jacobian $d\eta/dy$ obtained from Eq. (6) and the experimental data from [40].

analysis along the lines of [1]. We recapitulate the basic steps of the procedure:

(1) Each of the N_A and N_B wounded sources is associated with a longitudinally extended string.
(2) A string breaking at spatial rapidity y corresponds to a particle emission at rapidity y. The corresponding probability distribution for string breaking, $s(y; y_1, y_2)$, is uniform between the endpoints y_1 and y_2, namely $s(y; y_1, y_2) = \omega[\theta(y_1 < y < y_2) + \theta(y_2 < y < y_1)]$, where ω is a normalization constant and the function θ equals 1 wherever the condition in its argument is fulfilled, and 0 otherwise.
(3) String end points y_1 and y_2 follow distributions $g_1(y_1)$ and $g_2(y_2)$, respectively. The corresponding cumulative distribution functions (CDFs) are denoted as $G_1(y_1)$ and $G_2(y_2)$.

Then, the one-body emission profile $f(y)$ can be written as [1]

$$f(y) = \int_{-\infty}^{\infty} dy_1 \int_{-\infty}^{\infty} dy_2 g_1(y_1) g_2(y_2) s(y; y_1, y_2)$$
$$= \omega\left\{\frac{1}{2} - 2\left[G_1(y) - \frac{1}{2}\right]\left[G_2(y) - \frac{1}{2}\right]\right\}. \quad (8)$$

It is apparent from Eq. (8) that for a given one-body emission profile the solution to the string endpoint distributions $G_1(y)$ and $G_2(y)$ are not unique. It is, nevertheless, possible to constrain the range of possible solutions for the CDFs [1]. We denote y_0 as the position of the maximum of $f(y)$, and consider the two extreme cases:

(1) $f(y_0) = \omega/2$: In this case the string endpoint distributions $g_1(y)$ and $g_2(y)$ for both ends of the strings are identical. We label this case "$g_1 = g_2$." Of course, in this case also $G_1(y) = G_2(y)$.
(2) $f(y_0) = \omega$: In this case the supports for the string endpoint distributions $g_1(y)$ and $g_2(y)$ in rapidity are disjoint, hence we refer to this case as the "disjoint case." The distribution of the left endpoint, g_1, has support for $y \leqslant y_0$, whereas the distribution of the right endpoint, g_1, has support for $y \geqslant y_0$. Correspondingly, $G_1(y) = 1$ for $y \geqslant y_0$ and $G_2(y) = 0$ for $y \leqslant y_0$.

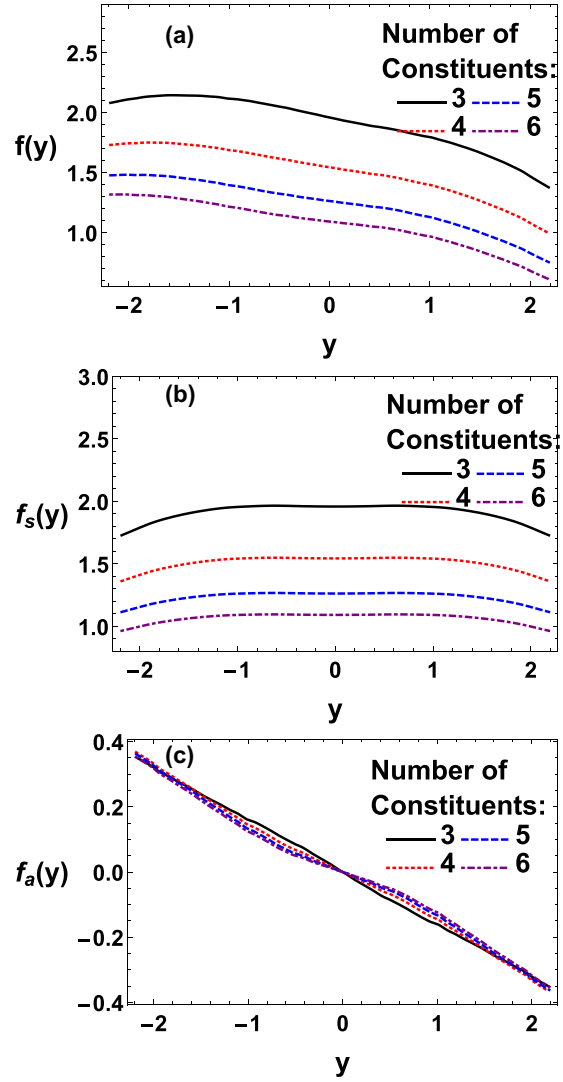

FIG. 7. Emission profiles of individual strings in rapidity for models with various numbers of wounded constituents (a) together with their respective symmetric (b) and antisymmetric parts (c).

Figure 8(a) shows these two limiting CDFs obtained with the profile $f(y)$ from Fig. 7 for the 5 parton case and Fig. 8(b) gives the corresponding string endpoint distributions, $g_1(y)$ and $g_2(y)$. The position of the maximum is $y_0 \simeq -2$. We note the desired features mentioned above. The disjoint case is interpreted in such a way that the left endpoint is always at $y \leqslant y_0$, essentially outside of the scope of the plot, whereas the right endpoint is smoothly distributed at $y \geqslant y_0$, with highest probability at high values of y. As discussed in Ref. [1], any solution of Eq. (8) must have $G_1(y)$ between the upper solid line and the dashed line, and $G_2(y)$ between the lower solid line and the dashed line in Fig. 8(a). This provides useful constraints that carry over to the analysis of two-body correlations.

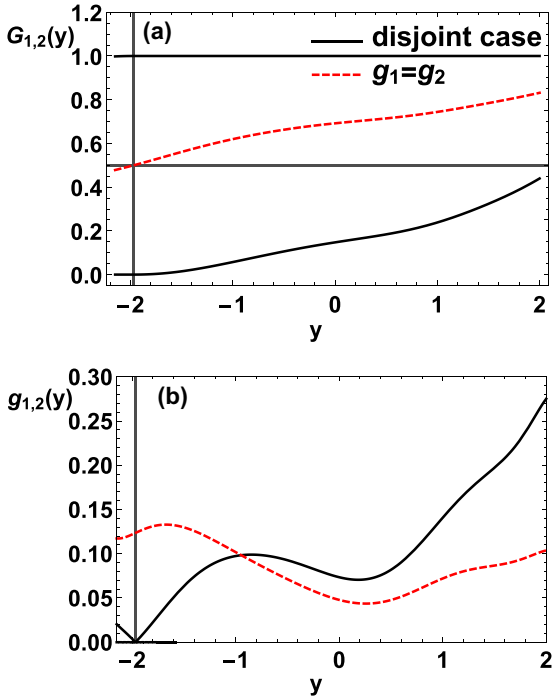

FIG. 8. Solutions for the cumulative distribution functions of string endpoints (a) and the corresponding probability distributions (b) in the $g_1 = g_2$ and disjoint cases (dashed and solid lines, respectively). Model with 5 constituent partons per nucleon.

V. TWO-PARTICLE CORRELATIONS

This section presents our model results for the two-particle correlations in pseudorapidity obtained for p-Pb and Pb-Pb collisions at $\sqrt{s_{NN}} = 5.02$ TeV. The findings presented here complement our earlier results [1] for d-Au and Au-Au collisions at $\sqrt{s_{NN}} = 200$ GeV, with the main difference that at $\sqrt{s_{NN}} = 5.02$ TeV a wounded parton model with 4 or 5 constituents per nucleon is used, rather than the model with 3 constituents per nucleon applied at $\sqrt{s_{NN}} = 200$ GeV.

The interesting feature that at higher collision energies one needs in the wounded picture more partons per nucleon has also been discussed in Refs. [29,34] within analyses of the particle multiplicities $dN_{\rm ch}/d\eta$ in A-A collisions. Our results are in line with the conclusion of [34], stating that whereas the fits at RHIC collision energies lead to 3 constituents partons, higher collision energies prefer about 5 partons per nucleon.

Two-particle correlations in A-B collisions are defined as

$$C_{\rm AB}(\eta_1, \eta_2) = \frac{\langle N(\eta_1, \eta_2)\rangle}{\langle N(\eta_1)\rangle\langle N(\eta_2)\rangle}, \tag{9}$$

where $N(\eta_1, \eta_2)$ is the number of pairs with one particle in a bin centered at η_1 and the other in a bin centered at η_2, and $N(\eta_i)$ is the number of particles in a bin centered at η_i. To the extent that $\eta \approx y$ (see the discussion in Sec. IV) and applying Eqs. (6) and (7), we may write

$$C_{\rm AB}(\eta_1, \eta_2) \approx C_{\rm AB}(y_1, y_2), \tag{10}$$

since the Jacobian factors $d\eta/dy$ cancel out between the numerator and denominator.

In analogy to the profile for the emission of individual particles from a single string, a two-particle profile for the emission of particle pairs from single strings is [1]

$$f_2(y_1, y_2) = \omega^2 G_1[\min(y_1, y_2)]\{1 - G_2[\max(y_1, y_2)]\} + (1 \leftrightarrow 2). \tag{11}$$

With this profile one obtains the correlation in pseudorapidity for particle pairs emitted from all strings in A-B collisions as

$$C_{\rm AB}(y_1, y_2) = 1 + \frac{{\rm cov}_{\rm AB}(y_1, y_2)}{f(y_1)f(y_2)}, \tag{12}$$

where ${\rm cov}_{\rm AB}(y_1, y_2)$ is

$$\begin{aligned} &{\rm cov}_{\rm AB}(y_1, y_2) \\ &= \langle N_A\rangle {\rm cov}(y_1, y_2) + \langle N_B\rangle {\rm cov}(-y_1, -y_2) \\ &\quad + {\rm var}(N_A) f(y_1) f(y_2) + {\rm var}(N_B) f(-y_1) f(-y_2) \\ &\quad + {\rm cov}(N_A, N_B)[f(y_1)f(-y_2) + f(-y_1)f(y_2)]. \end{aligned} \tag{13}$$

Contributions to this expression come from emission of a hadron pair from the same string (associated with a wounded parton in A or B nucleus) and from the case where the two hadrons originate from different strings.

We emphasize that while the different string endpoint distributions found in the previous section yield the same one-body emission spectra by construction, the same is not in general true for the corresponding two-particle correlations. Indeed, noticeable differences occur, as can be seen in Fig. 9, where results for $C_{\rm AB}(\eta_1, \eta_2) \simeq C_{\rm AB}(y_1, y_2)$ in both the $g_1 = g_2$ and the disjoint cases are shown: Both cases yield correlations with a ridgelike structure along the $\eta_1 = \eta_2$ direction. However, for the $g_1 = g_2$ case the ridge is higher than that of the disjoint case and thus exhibits a steeper decrease in the $\eta_1 = -\eta_2$ direction. We found the same qualitative behavior also for correlations from d-Au and Au-Au collisions at 200 GeV [1]. For comparison, we also show in Fig. 9(c) the results for the 4 constituent model in the disjoint case, which is close to the 5 constituent case from panel (b).

To analyze $C_{\rm AB}(y_1, y_2)$ in more quantitative detail, we also study its projections on the Legendre polynomials [44]

$$a_{nm} = \frac{\int_{-Y}^{Y} dy_1 \int_{-Y}^{Y} dy_2 C(y_1, y_2) T_n\left(\frac{y_1}{Y}\right) T_m\left(\frac{y_2}{Y}\right)}{\int_{-Y}^{Y} dy_1 \int_{-Y}^{Y} dy_2 C(y_1, y_2)}, \tag{14}$$

where we follow the choice of $Y = 2.4$ of the ATLAS Collaboration in order to be able to compare with their results. The dominant contributions to $C_{\rm AB}(y_1, y_2)$ are represented by the a_{11} coefficients. Our model results for p-Pb and Pb-Pb collisions at $\sqrt{s_{NN}} = 5.02$ TeV are shown in Fig. 10 as a function of the number of charged particles $N_{\rm ch}$ that are produced within the collisions. As expected, the larger fall-off from the ridge for the correlations in the $g_1 = g_2$ case is reflected in larger a_{11} coefficients. Our results are shown in comparison to values extracted from ATLAS data for Pb-Pb collisions at $\sqrt{s_{NN}} = 2.76$ TeV and p-Pb collisions

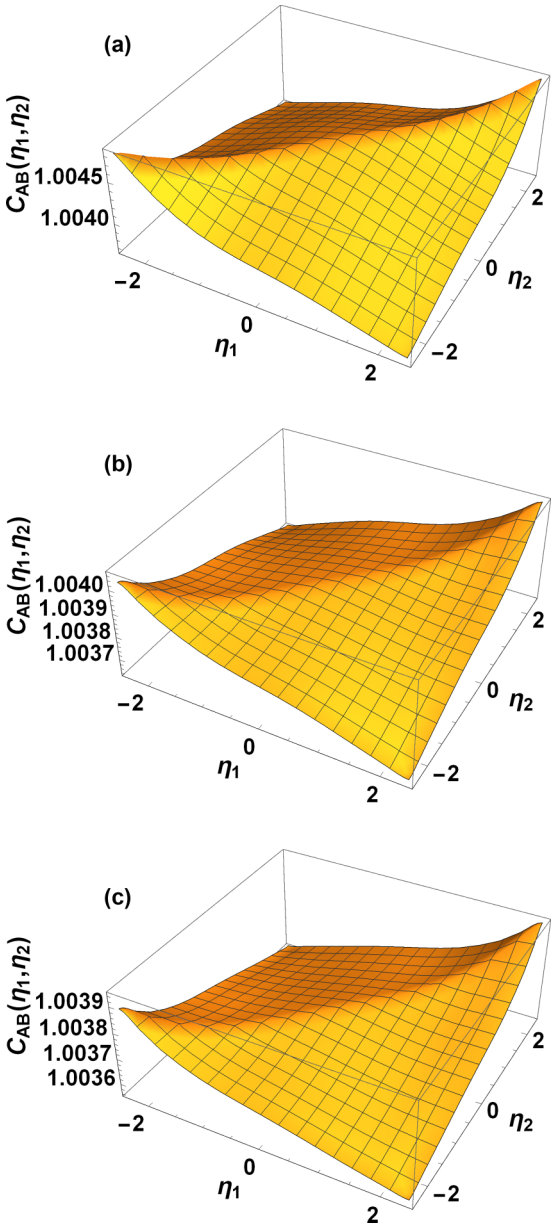

FIG. 9. Correlations $C(\eta_1, \eta_2)$ in pseudorapidity for the $g_1 = g_2$ (a) and the disjoint (b) cases for the 5% most central Pb-Pb collisions at $\sqrt{s_{NN}} = 5.02$ TeV for the model with 5 constituent partons per nucleon. In (c) the disjoint case for the model with 4 constituent partons per nucleon is shown.

at $\sqrt{s_{NN}} = 5.02$ TeV from [45]. We use the data for a_{11} subtracted by the contribution coming from the short range interactions.

To show our model results as functions of $\langle N_{\rm ch}\rangle$ rather than $\langle N_+\rangle$, we infer from Eq. (2) that

$$\langle N_{\rm ch}\rangle = \langle N_+\rangle \int_{-Y}^{Y} d\eta\, f_s(\eta). \tag{15}$$

From this relation we obtain the proportionality $\langle N_{\rm ch}\rangle = 5.76\langle N_+\rangle$ and $\langle N_{\rm ch}\rangle = 5.43\langle N_+\rangle$ in the case of p-Pb and Pb-Pb collisions, respectively (both with 5 constituents per nucleon). For the 4 constituent model the corresponding values are

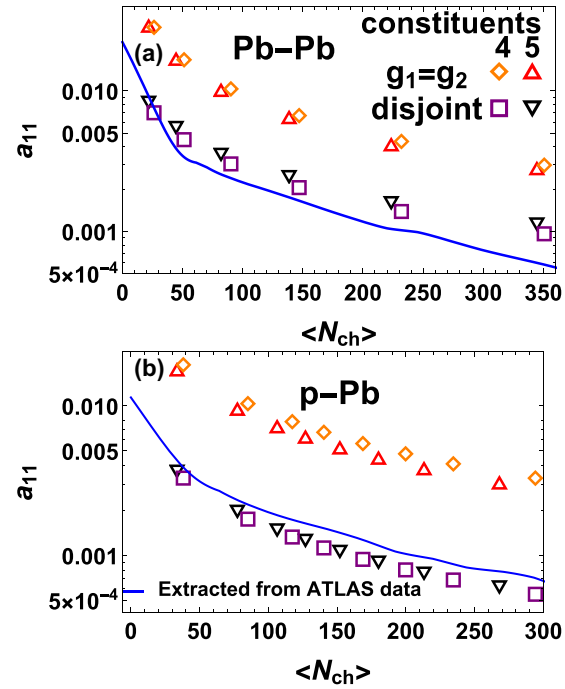

FIG. 10. Model results for the coefficients a_{11} for Pb-Pb (a) and p-Pb (b) collisions at $\sqrt{s_{NN}} = 5.02$ TeV, corresponding to the $g_1 = g_2$ and disjoint cases, plotted as functions of the number of charged particles $N_{\rm ch}$ (points), in comparison to experimental data from ATLAS [45] (solid line) at $\sqrt{s_{NN}} = 2.76$ TeV and at $\sqrt{s_{NN}} = 5.02$ TeV for Pb-Pb and p-Pb collisions respectively. Models with 4 and 5 constituent partons per nucleon.

$\langle N_{\rm ch}\rangle = 6.97\langle N_+\rangle$ and $\langle N_{\rm ch}\rangle = 6.64\langle N_+\rangle$ for p-Pb and Pb-Pb collisions, respectively.

We note from Fig. 10 that the model results for the a_{11} coefficient for the disjoint case are close to the ATLAS data, compared to the $g_1 = g_2$ case which largely overestimates the data by about a factor of 4. We alert the reader that for the Pb-Pb there is a mismatch in the collision energy, as the model analysis is carried for $\sqrt{s_{NN}} = 5.02$ TeV, while the data are available for $\sqrt{s_{NN}} = 2.76$ TeV. Numerically, the mismatch is not significant. For comparison, we show in Fig. 10 the results for the 4 and 5 constituent models, which are very close to each other.

We note that the model results for a_{11} scale approximately as $1/N_{\rm ch} \sim 1/N_+$, as follows from Eqs. (12) and (13). Speaking of the decomposition (13), it is interesting to separate the $\langle N_A\rangle {\rm cov}(y_1, y_2) + \langle N_B\rangle {\rm cov}(-y_1, -y_2)$ term originating from intrinsic correlations of emission from a string, from the remainder coming from the fluctuation of the number of strings. Following [1], we denote the corresponding Legendre coefficient as a^*_{11}. Then the ratio a^*_{11}/a_{11} is a measure of the intrinsic correlations compared to the total. This ratio is plotted in Fig. 11 for the models with 4 and 5 constituents as a function of the number of produced charged particles $N_{\rm ch}$, for both p-Pb and Pb-Pb collisions. As can be seen, for the disjoint case which is close to the data, for Pb-Pb the ratio is around 0.4, indicating a comparable share of the contributions from intrinsic string endpoint fluctuations and the fluctuation

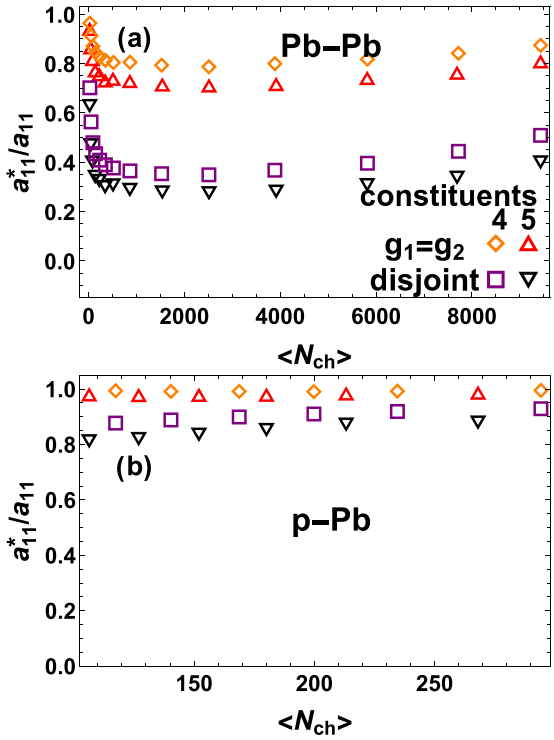

FIG. 11. Ratios a^*_{11}/a_{11} for Pb-Pb (a) and p-Pb (b) collisions at $\sqrt{s_{NN}} = 5.02$ TeV as functions of the number of charged particles $N_{\rm ch}$. Models with 4 and 5 constituent partons per nucleon.

of the number of strings. For the p-Pb case, the corresponding ratio is above 0.8, thus the intrinsic fluctuations dominate here.

VI. p-p COLLISIONS

With the nucleon substructure present in the model with several constituent partons, it is possible to carry out the correlation analysis also for the p-p collisions. In doing so, we use the same emission profile $f(\eta)$ obtained earlier from fitting the Pb-Pb and p-Pb pseudorapidity spectra at $\sqrt{s_{NN}} = 5.02$ TeV. As before, the numbers of wounded partons are obtained with GLISSANDO3 [39] and the negative binomial distribution is overlaid according to Eq. (3). The results, compared to ATLAS data [45] at $\sqrt{s_{NN}} = 13$ TeV, are presented in Fig. 12. We note a fair agreement between the model and the experiment, again for the disjoint case. Again, the cases with 4 and 5 partons per nucleon are close to each other.

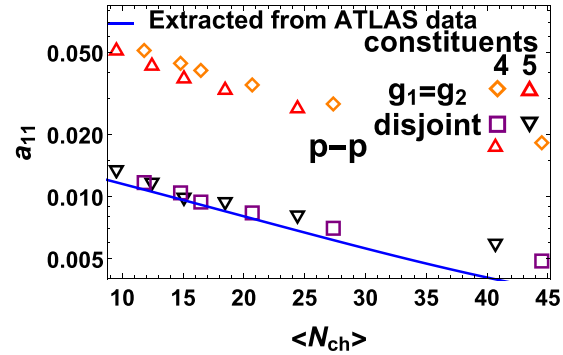

FIG. 12. The Legendre coefficient a_{11} for p-p collisions at $\sqrt{s_{NN}} = 5.02$ TeV, in comparison to the ATLAS data [45] at $\sqrt{s_{NN}} = 13$ TeV. Models with 4 and 5 constituent partons per nucleon.

VII. SUMMARY AND CONCLUSIONS

The basic conclusion of our study is that a very simple semianalytic approach involving strings of fluctuating endpoints is capable of explaining the basic features of the long-range two-particle correlation data in pseudorapidity, as measured by the ATLAS Collaboration [45]. In particular, the model with 4 or 5 constituent partons per nucleon and the disjoint distributions for the two fluctuating endpoints reasonably describes the data for Pb-Pb, p-Pb, and p-p collisions. This explains why more sophisticated models incorporating the string breaking mechanism, such as those used in various popular Monte Carlo generators, work in describing the longitudinal correlations.

Our approach merges the wounded constituent model with a generic description of string breaking that was first presented in Refs. [2] and [1], and used for nuclear collisions at $\sqrt{s_{NN}} = 200$ GeV at RHIC. The extension to LHC energies, presented here for $\sqrt{s_{NN}} = 5.02$ TeV, seems phenomenologically successful. Further tests of the model could be performed when the experimental correlation analysis at other collision energies, with broader pseudorapidity coverage, and for other systems become available.

ACKNOWLEDGMENT

This research was supported by the Polish National Science Centre (NCN) under Grant No. 2015/19/B/ST2/00937.

[1] M. Rohrmoser and W. Broniowski, Phys. Rev. C **99**, 024904 (2019).
[2] W. Broniowski and P. Bożek, Phys. Rev. C **93**, 064910 (2016).
[3] B. Andersson, G. Gustafson, G. Ingelman, and T. Sjostrand, Phys. Rep. **97**, 31 (1983).
[4] X.-N. Wang and M. Gyulassy, Phys. Rev. D **44**, 3501 (1991).
[5] Z.-W. Lin, C. M. Ko, B.-A. Li, B. Zhang, and S. Pal, Phys. Rev. C **72**, 064901 (2005).
[6] T. Sjöstrand, S. Ask, J. R. Christiansen, R. Corke, N. Desai, P. Ilten, S. Mrenna, S. Prestel, C. O. Rasmussen, and P. Z. Skands, Comput. Phys. Commun. **191**, 159 (2015).
[7] C. Bierlich, G. Gustafson, L. Lönnblad, and H. Shah, J. High Energy Phys. 10 (2018) 134.
[8] S. Ferreres-Solé and T. Sjöstrand, Eur. Phys. J. C **78**, 983 (2018).
[9] A. Capella, U. Sukhatme, C.-I. Tan, and J. Tran Thanh Van, Phys. Rep. **236**, 225 (1994).
[10] K. Werner, I. Karpenko, T. Pierog, M. Bleicher, and K. Mikhailov, Phys. Rev. C **82**, 044904 (2010).
[11] T. Pierog, I. Karpenko, J. Katzy, E. Yatsenko, and K. Werner, Phys. Rev. C **92**, 034906 (2015).
[12] A. Białas, M. Błeszyński, and W. Czyż, Nucl. Phys. B **111**, 461 (1976).

[13] R. J. Glauber, in *Lectures in Theoretical Physics*, edited by W. E. Brittin and L. G. Dunham (Interscience, New York, 1959), Vol. 1, p. 315.
[14] W. Czyż and L. C. Maximon, Ann. Phys. (NY) **52**, 59 (1969).
[15] A. Białas, W. Czyż, and W. Furmański, Acta Phys. Pol. B **8**, 585 (1977).
[16] A. Białas, K. Fiałkowski, W. Słomiński, and M. Zieliński, Acta Phys. Pol. B **8**, 855 (1977).
[17] A. Białas and W. Czyż, Acta Phys. Pol. B **10**, 831 (1979).
[18] V. V. Anisovich, Yu. M. Shabelski, and V. M. Shekhter, Nucl. Phys. B **133**, 477 (1978).
[19] S. Eremin and S. Voloshin, Phys. Rev. C **67**, 064905 (2003).
[20] P. K. Netrakanti and B. Mohanty, Phys. Rev. C **70**, 027901 (2004).
[21] A. Białas and A. Bzdak, Phys. Lett. B **649**, 263 (2007).
[22] A. Białas and A. Bzdak, Phys. Rev. C **77**, 034908 (2008).
[23] B. Alver, M. Baker, C. Loizides, and P. Steinberg, arXiv:0805.4411.
[24] G. Agakishiev *et al.* (STAR Collaboration), Phys. Rev. C **86**, 014904 (2012).
[25] S. S. Adler *et al.* (PHENIX Collaboration), Phys. Rev. C **89**, 044905 (2014).
[26] C. Loizides, J. Nagle, and P. Steinberg, SoftwareX **1–2**, 13 (2015).
[27] A. Adare *et al.* (PHENIX Collaboration), Phys. Rev. C **93**, 024901 (2016).
[28] R. A. Lacey, P. Liu, N. Magdy, M. Csanád, B. Schweid, N. N. Ajitanand, J. Alexander, and R. Pak, Universe **4**, 22 (2018).
[29] P. Bożek, W. Broniowski, and M. Rybczyński, Phys. Rev. C **94**, 014902 (2016).
[30] L. Zheng and Z. Yin, Eur. Phys. J. A **52**, 45 (2016).
[31] E. K. G. Sarkisyan, A. N. Mishra, R. Sahoo, and A. S. Sakharov, Phys. Rev. D **94**, 011501(R) (2016).
[32] J. T. Mitchell, D. V. Perepelitsa, M. J. Tannenbaum, and P. W. Stankus, Phys. Rev. C **93**, 054910 (2016).
[33] O. S. K. Chaturvedi, P. K. Srivastava, A. Kumar, and B. K. Singh, Eur. Phys. J. Plus **131**, 438 (2016).
[34] C. Loizides, Phys. Rev. C **94**, 024914 (2016).
[35] M. J. Tannenbaum, Mod. Phys. Lett. A **33**, 1830001 (2017).
[36] M. Barej, A. Bzdak, and P. Gutowski, Phys. Rev. C **97**, 034901 (2018).
[37] M. Barej, A. Bzdak, and P. Gutowski, Phys. Rev. C **100**, 064902 (2019).
[38] A. Białas and W. Czyż, Acta Phys. Pol. B **36**, 905 (2005).
[39] P. Bożek, W. Broniowski, M. Rybczyński, and G. Stefanek, Comput. Phys. Commun. **245**, 106850 (2019).
[40] J. Adam *et al.* (ALICE Collaboration), Phys. Lett. B **772**, 567 (2017).
[41] G. Aad *et al.* (ATLAS Collaboration), Eur. Phys. J. C **76**, 199 (2016).
[42] B. B. Back *et al.* (PHOBOS Collaboration), Phys. Rev. C **65**, 031901 (2002).
[43] J. Adam *et al.* (ALICE Collaboration), Phys. Rev. C **91**, 064905 (2015).
[44] A. Bzdak and D. Teaney, Phys. Rev. C **87**, 024906 (2013).
[45] M. Aaboud *et al.* (ATLAS Collaboration), Phys. Rev. C **95**, 064914 (2017).